Proof of Concept of Model-based Cardiovascular Prediction

Call identifier: FP7-ICT-2013-10 - **Grant agreement no**: 611232

Thematic Priority: ICT-2013.5.2: Virtual Physiological Human

Deliverable 7.1

Computational tool for computing the pressure-difference field from 4D Flow data

Due date of delivery: 30th September 2014

Actual submission date: 3rd October 2014

Start of the project: 1st October 2013
Ending Date: 30th September 2016

Partner responsible for this deliverable: Siemens AG

Version: Final

Dissemination Level: Restricted to a group specified by the consortium (including the Commission Services)

Document Classification

Title	Computational tool for computing the pressure-difference field from 4D Flow data
Deliverable	D7.1
Reporting Period	1
Authors	Olivier Ecabert
Work Package	WP7
Security	Restricted to a group specified by the consortium (including the Commission Services)
Nature	Report
Keyword(s)	4D Flow, Aorta, Phase Contrast MRI, Poisson Equation, Pressure, Simulation, Valve Disease, Velocity Field

Document History

Name	Remark	Version	Date
Olivier Ecabert		Final	30th Sept. 2014

List of Contributors

Name	Affiliation
Olivier Ecabert	Siemens AG

List of reviewers

Name	Affiliation
Anja Hennemuth	Fraunhofer MEVIS
Paul Groenenboom	ESI-Group

Abbreviations

2D	Two-Dimensional
3D	Three-Dimensional
4D	Four-Dimensional
AVD	Aortic Valve Disease
BC	Boundary Conditions
CFD	Computational Fluid Dynamics
CoA	Coarctation
FCP	Flux-Constrained Poisson
MIP	Maximum Intensity Projection
MRI	Magnetic Resonance Imaging
PC	Phase Contrast
PCMRA	Phase-Contrast MR Angiography

PPE	Pressure Poisson Equations
VENC	Velocity Encoded Gradient Echo Imaging
WP	Work Package

Contents

Executive Summary

This deliverable reports on a method developed to compute the relative pressure within the aorta non-invasively from magnetic resonance imaging (MRI). The proposed approach is two-fold. In the first step, the blood velocity acquired by phase contrast MRI is reconstructed from the measurements as it is not discretely incompressible and suffers from various artefacts, especially near the vessel walls. The second step takes the reconstructed velocities to compute the time-varying 3D relative pressure within the aorta using the Poisson equation. The implementation is based on a level-set based embedded boundary method which eliminates the need for a time consuming manual generation of a numerical discretization grid (i.e. volumetric mesh), thereby easing the overall workflow. Finally, we applied the whole pipeline on three patients of the CARDIOPROOF database with valve disease and analysed the resulting relative pressure.

Introduction

Clinical Background and Motivation

Both aortic valve disease (AVD) addressed in WP5 and aortic coarctation (CoA) addressed in WP6 are strictly connected to the morphology of the aortic arch. Aortic arch dilatation occurs frequently and at a young age in patients with aortic disease.

Increased aortic arch stress (of both tensile and shear type) plays a role in pathogenesis of aortic wall remodelling and dilation. Both exert forces to the aortic wall that trigger cellular signalling cascades resulting in increased expression of growth factors or nitric oxide. These factors influence, among others, the vascular wall matrix which can result in aortic dilation or atherosclerosis.

Aortic valve disease strongly interacts with aortic dilation, as regurgitant valves have higher stroke volumes leading to higher wall tension in the ascending aorta, thus the severity of aortic regurgitation correlates with the degree of aortic root dilatation. There may be a bimodal effect, with increasing root dilatation leading to poor leaflet coaptation and thus more regurgitation. In contrast stenotic valves create a high-velocity jet that increases shear stress on the anterolateral portion of the ascending aorta.

Rates of growth of the ascending aorta in the presence of aortic valve disease vary within studies, although it is known that larger aortas have faster expansion rates. One study demonstrated that expansion rate was ≈2.1 mm/y for those with an initial diameter of 35 to 40 mm and 5.6 mm/y for aneurysms ≥60 mm. Both paediatric and adult studies have demonstrated significantly faster aortic dilatation with bicuspid aortic valve as compared to tricuspid aortic valves. Independently of the type of aortic disease, aortic dilation is also a significant predictor of dissection and rupture (acute cardiovascular events leading to death if untreated), thus evolution of aortic arch dilation after surgery for CoA or AVD is also important for prognostics.

Knowledge of pressure and velocity of blood flow in the human cardiovascular system can be decisive for clinical evaluations (initial and post-procedural) and procedure planning. For example, the severity of the cardiovascular diseases targeted in this project (CoA and AVD) can be assessed by intraluminal pressure gradients (Currie, et al. 1985).

In the context of this work, non-invasive time-resolved 3D phase contrast (PC) magnetic resonance imaging (MRI) with three-directional velocity encoding (also referred to as 4D flow MRI) (Markl, et al. 2007) (Markl, Kilner and Ebbers 2011) provides in-vivo blood velocity information that can be combined with biophysical

models of the vessels to derive intraluminal relative pressures (Figure 1). This approach offers a full 3D+time computation of the relative pressure, which can then be used to estimate temporal and spatial gradients within a vessel segment.

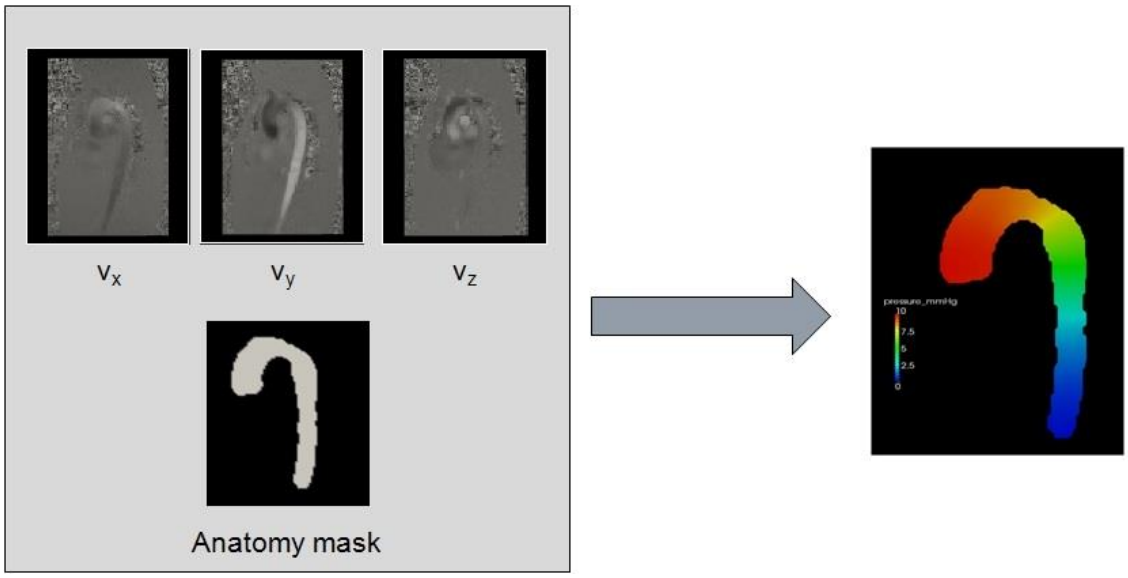

Figure 1 Schematic representation of the overall approach to derive relative pressure from non-invasive PC-MRI data

Proposed Workflow

In this report, we present an efficient workflow for the computation of relative pressure from 4D flow MRI summarized in Figure 2.

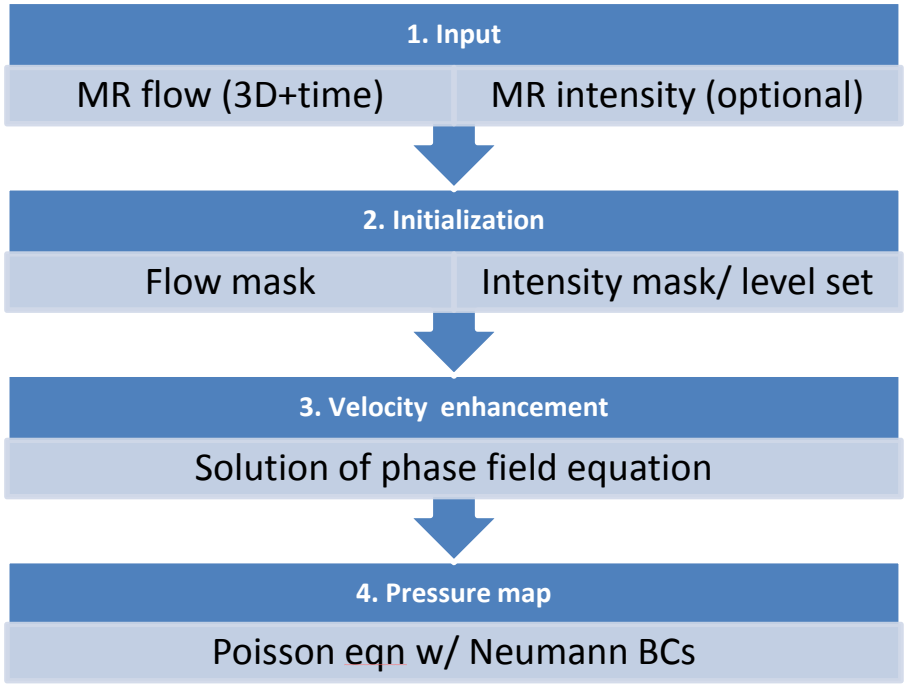

Figure 2 Main steps of the proposed workflow to derive relative pressure maps from PC-MRI data.

The only input to the workflow is a complete PC-MRI data set (step 1). The computational domain (aorta and sub-clavian arteries) can be extracted from the PC-MRI data set using semi-automatic segmentation. The resulting mask is then tagged (inlet/outlet/wall), smoothed, and converted into a level set allowing for higher accuracy computation (step 2).

The first major component is in the reconstruction of blood flow velocity from the original 4D flow MR images (step 3). Indeed, the velocity field measured in 4D flow MRI is not discretely incompressible, and suffers from various aliasing and noise artefacts, especially near the wall. Therefore, we perform a correction step including background phase correction (mitigating Eddy current artefacts) and then VENC anti-aliasing prior to solving a Poisson equation that enhances the velocity field ensuring the conservation of flux.

The second major component is in deriving the pressure map from the reconstructed velocity field (step 4). Here, we solve the Pressure Poisson Equation (PPE) obtained by taking the divergence of the Navier-Stokes momentum balance equation, and imposing the natural Neumann boundary conditions (see Section Quantification of Pressure Maps from Phase-Contrast MRI below in the text).

In summary, our workflow consists of an integrated framework for data processing and computation that enables the user to progress through the data processing pipeline in a fast, semi-automatic, intuitive fashion, and to obtain the final result in a matter of minutes. Each step is described in details in the next sections, followed by a first evaluation of the overall workflow on the data sets currently available.

Blood Flow Velocity Reconstruction from Medical Images

Previous Work

There are several technologies (e.g. PC-MRI, Cine MR, Doppler ultrasound, Particle Image Velocimetry, etc) that can be used to measure flow inside a bounded cavity be it industrial in nature (pipe or tank of fluid) or biological (blood vessel, heart, etc). Velocity data reported by any of these technologies can suffer from noise artefacts that move the velocity field out of the space of divergence free vector fields, i.e. the mass is not conserved. There are a number of methods that address this problem (Busch, et al. 2012) (Meier, et al. 2013) (Song and Leahy 1991) (Song, Napel, et al. 1993) (S. M. Song, R. M. Leahy, et al. 1994) (Tafti and Unser 2011) (Tafti, Delgado-Gonzalo, et al. 2011).

Several previous works that consider the issue of velocity reconstruction from measured data use various techniques which essentially act as enhancement filters in order to enforce incompressibility of the given velocity field. Such filters are either global or, more commonly, have compact support (Busch, et al. 2012) (Meier, et al. 2013) (Krittian, et al. 2012) (Song and Leahy 1991) (Song, Napel, et al. 1993) (S. M. Song, R. M. Leahy, et al. 1994), given by voxel masks approximating the region of interest.

These previous methods do not attempt to use any knowledge of the inlet/outlet flux distributions or wall deformation. Due to this limiting approach, one cannot impose the correct outlet flux when one has multiple outlets, and the old methods can only work with one inlet-one outlet data. This is quite different from a vessel or pipe network, as is for example the aorta together with the supra-aortic arteries. In contrast with our reconstruction method, previous methods do not identify exact wall, inlet or outlet location, and therefore are limited to using Dirichlet boundary conditions either far away outside these locations, or several grid cells inside (Song, Napel, et al. 1993) (S. M. Song, R. M. Leahy, et al. 1994) (Song

and Leahy 1991) (Meier, et al. 2013). As a consequence, various artefacts may appear, e.g. a stationary wall flux may be nonzero, or the total boundary flux is not being conserved.

Velocity Reconstruction Approach

Velocity, as measured using PC-MRI or other methods, is not discretely incompressible, and suffers from various aliasing and noise artefacts, especially near the walls (due to jumps in the density across the wall). We define a corrected velocity field, U^{new} as:

$$U^{new} = U^{measured} - \nabla\lambda \tag{1}$$

where λ is a potential function. Applying the divergence operator and requiring the new velocity field to be incompressible, we get the following Poisson's equation for the potential field:

$$\Delta\lambda = \nabla \cdot U^{measured} \tag{2}$$

The Neumann boundary conditions compatible with (1) can be obtained by projecting (2) in the direction normal to the boundary:

$$\frac{\partial\lambda}{\partial n} = (U^{measured} - U^{new}) \cdot n \tag{3}$$

Obviously, once we solve (2+3) we have $\int_{\partial D} U^{new} \cdot n = 0$, which is simply the condition that the total flux through the boundaries of the domain is conserved. If the walls are rigid, this condition simply states that the flow coming in through the domain inlets is the same as the flow leaving through the domain outlets.

We note that the elliptic system (2+3) allows us to use in principle any prescribed flux $\int_A U^{new} \cdot n$ through a surface *A* (inlet, outlet or wall), as long as the global sum satisfies mass conservation $\sum_{A_i} \int_{A_i} U^{new} \cdot n = 0$, where we assume that the domain *D* is an oriented manifold, and *n* is the unit field normal to the boundary. The main component of this approach consists in using such prescribed fluxes as constraints for the boundary velocity U^{new}, subject to mass conservation, and using this constrained U^{new} further on to specify the boundary conditions (3). Let us formalize this as the Flux-Constrained Poisson equations (FCP):

$$\begin{cases} \Delta\lambda = \nabla \cdot U^{measured} & (4.1) \\ \dfrac{\partial\lambda}{\partial n} = (U^{measured} - U^{B}) \cdot n & (4.2) \\ \displaystyle\int_{A_i} U^{B} \cdot n = f_i & (4.3) \\ \displaystyle\sum_{A_i} f_i = 0 & (4.4) \end{cases}$$

Relations (4.3-4.4) are prescribed mass conservation conditions for the boundary velocity U^B, and they ensure that $\int_{\partial D} \frac{\partial\lambda}{\partial n} = \int_{\partial D} U^{measured} \cdot n$, which is the necessary compatibility condition for the Poisson equation with Neumann boundary conditions (4.1-4.2). The boundary velocity U^B is either measured or needs to be prescribed such that it observes the total flux conservation (4.4). The advantage of solving the FCP equations consists in being able to recover a "physically realistic velocity field". We mean by this that even though the measured flow may be clearly wrong from the point of view of global flux conservation through the boundaries, one can adjust the boundary conditions such that they do ensure boundary flux conservation. This can be very useful for example when one uses defective data coming from modalities

like Flow MRI or Doppler ultrasound, in which the inlet flux does not match the sum of outlet fluxes. We note that (Song, Napel, et al. 1993) and (Meier, et al. 2013) solve a system of the type (4) but use $U^B = 0$, which does not impose any constraints on fluxes at the domain boundaries. As a consequence, the resulting velocity field obtained from the relation (1) is not guaranteed to conserve boundary flux, and furthermore this introduces (possibly large) errors when the velocity field is subsequently used for determination of the relative pressure field.

Using a variational calculus , one can show that solving (4) is equivalent to solving the minimization problem $argmin_\lambda(\left|\left|\nabla\lambda - U^{measured} + U^B\right|\right|_2^2$, where U^B is chosen to be divergence free and satisfying (4.3-4.4). Details can be found in (S. M. Song, R. M. Leahy, et al. 1994).

Workflow for Blood Flow Velocity Reconstruction

In this section, we present the steps of the workflow for blood flow velocity reconstruction that are implemented as part of the prototype referred to as 4D Flow Tool later in this report (Gülsün, Jolly, et al. 2012).

1. Extraction of Aortic Centreline and Lumen from PC-MRI Data

Depending on the quality of the PC-MRI measurements, the underlying data set (“3D angiography volume”) used for lumen segmentation can be chosen by the used to be either the magnitude contrast averaged over all timeframes or the phase-contrast angiography (PCMRA) contrast averaged over all timeframes or the temporal MIP of the PCMRA contrast or the time-resolved magnitude contrast or the time-resolved PCMRA.

The vascular modelling method first detects a centreline tree representation between user-placed seeds (Figure 3 and Figure 4) in one of the volumes mentioned above and then extracts the lumen boundary using the detected centrelines (Figure 5). The centreline extraction method is based on a minimal path detection algorithm which operates on a medialness map which is computed by contrast and scale independent filters using 2D multi-scale cross-sectional models and then integrated into a discrete optimization framework for centreline tracking (Gülsün and Tek, Robust vessel tree modeling 2008). The lumen extraction method is based on graph-cuts optimization technique using centrelines as input. It first constructs a tubular 3D grid graph in the vicinity of the input centreline with the integration of normalized boundary properties measured by multi-scale mean shift filters and then finds a smooth surface with globally optimum energy (Gülsün and Tek 2010).

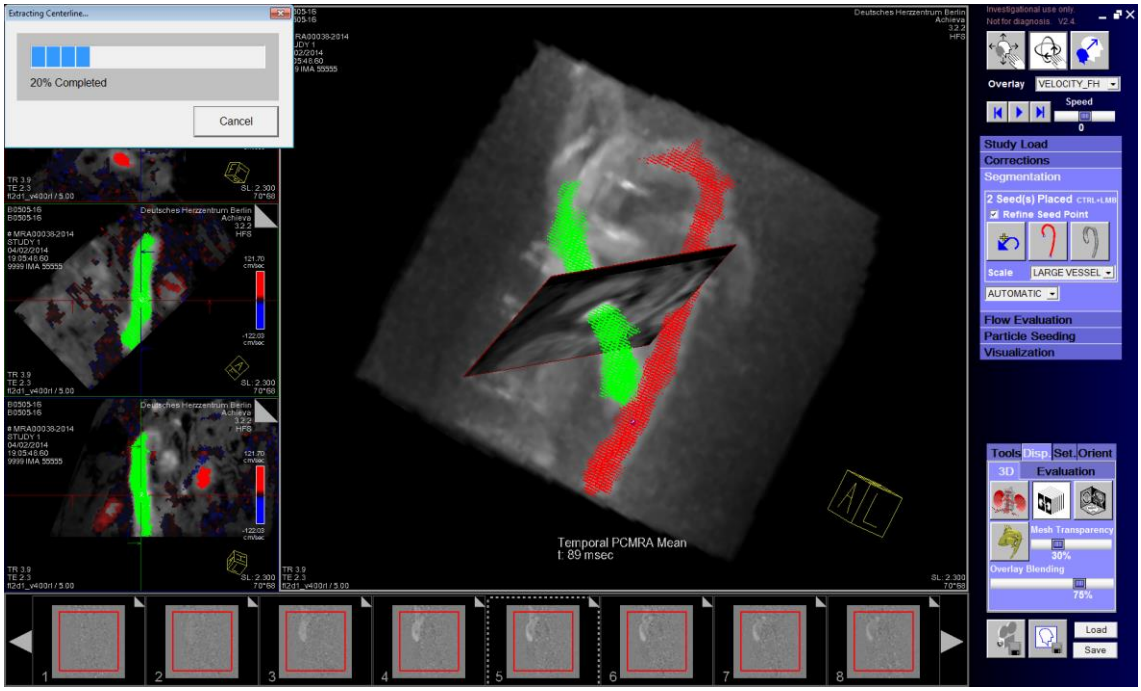

Figure 3 Seeds manually placed in the green and red regions within the aorta are propagated to allow centerline extraction.

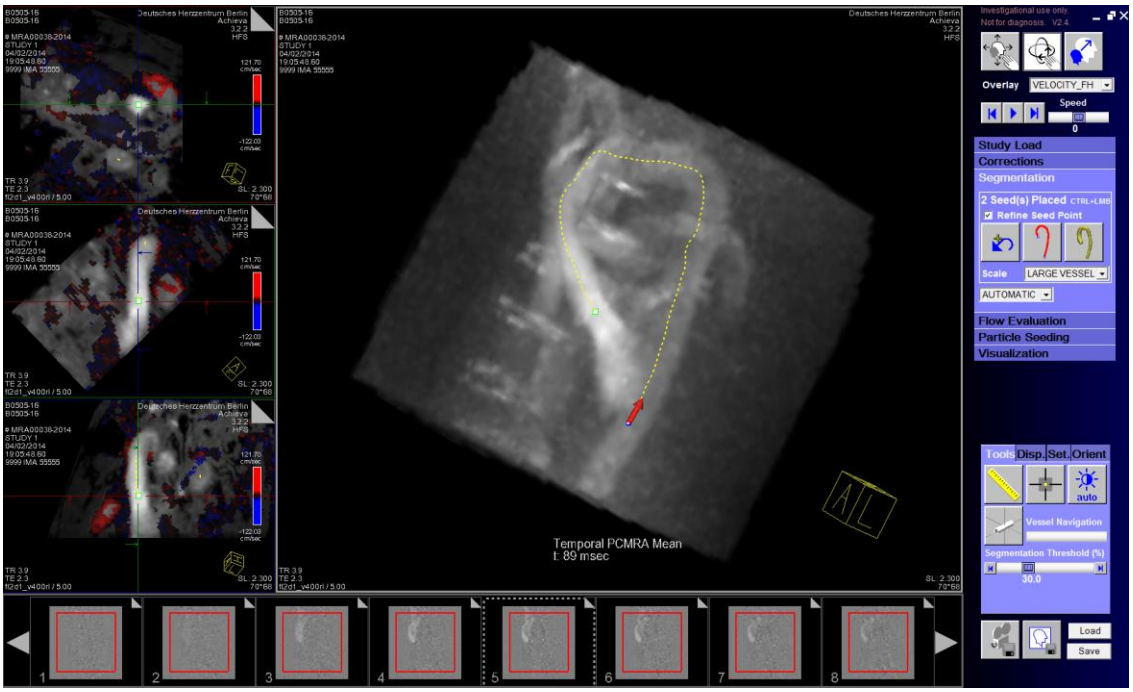

Figure 4 The aortic centerline is extracted from the mask obtained from the previous step.

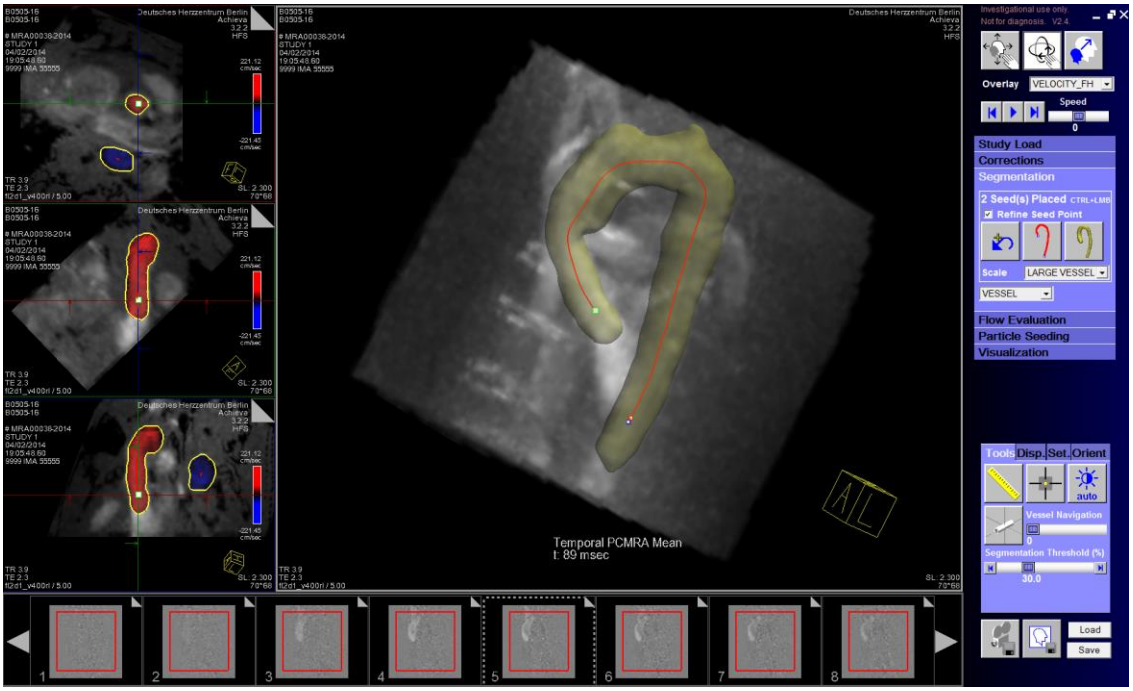

Figure 5 Lumen segmentation.

2. Extraction of Regular Aortic Walls and Definition of Inlets/Outlets

We increase the regularity of the extracted lumen by converting the 3D binary mask into an iso-surface (Figure 6). Then, we smooth the resulting mesh with a volume preserving algorithm (Taubin smoothing with λ=0.33 and μ=-0.331 (Taubin 1995)) (Figure 7). This ensures on one hand that local high curvature variations are removed while smaller vessels (e.g. supra-aortic arteries) are not shrunk such as with Laplace smoothing approaches. Finally, the vessel surface is interactively cut and each cross-section is tagged either as inlet, wall or outlet (Figure 8). Figure 9 demonstrates the higher mesh quality of the proposed approach compared to a surface derived from a generic voxelization algorithm; compare for example the local surface curvature.

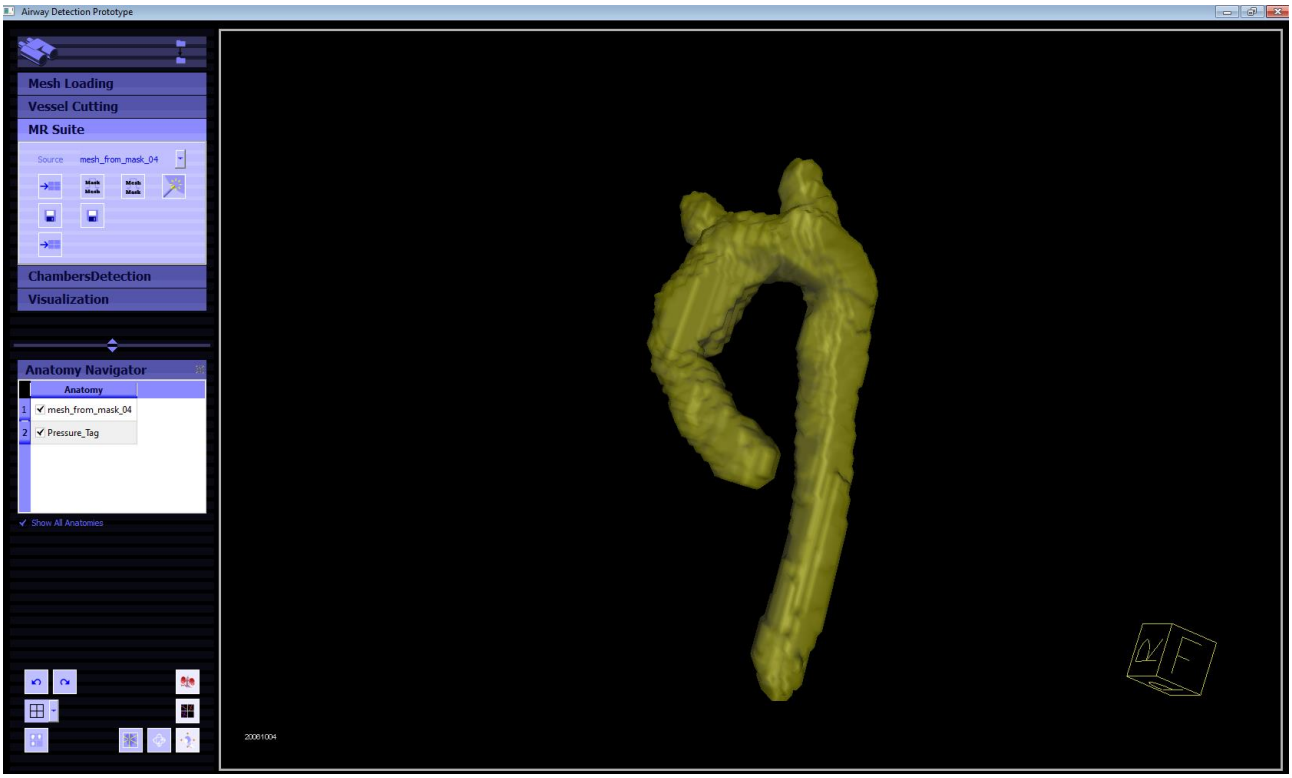

Figure 6 Converting the volumetric mask of the aortic lumen into a surface mesh.

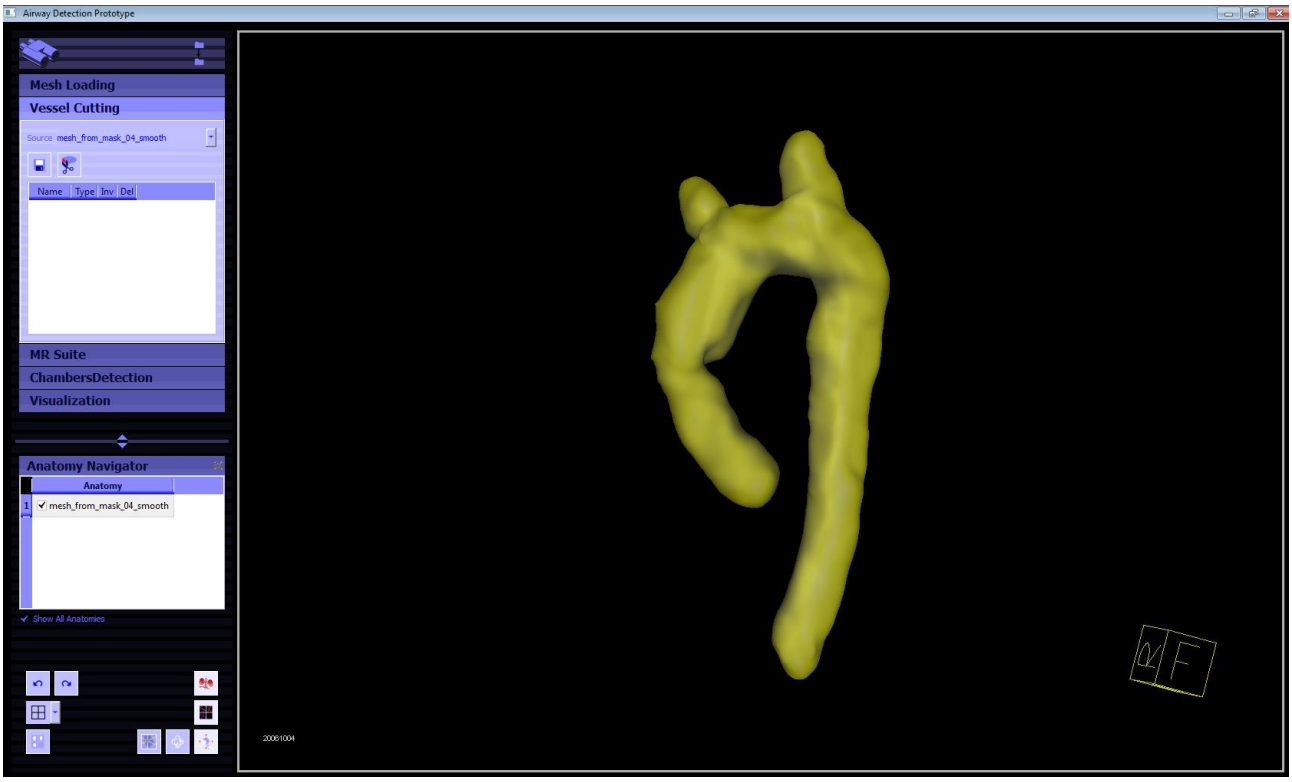

Figure 7 Mesh smoothing with volume preservation.

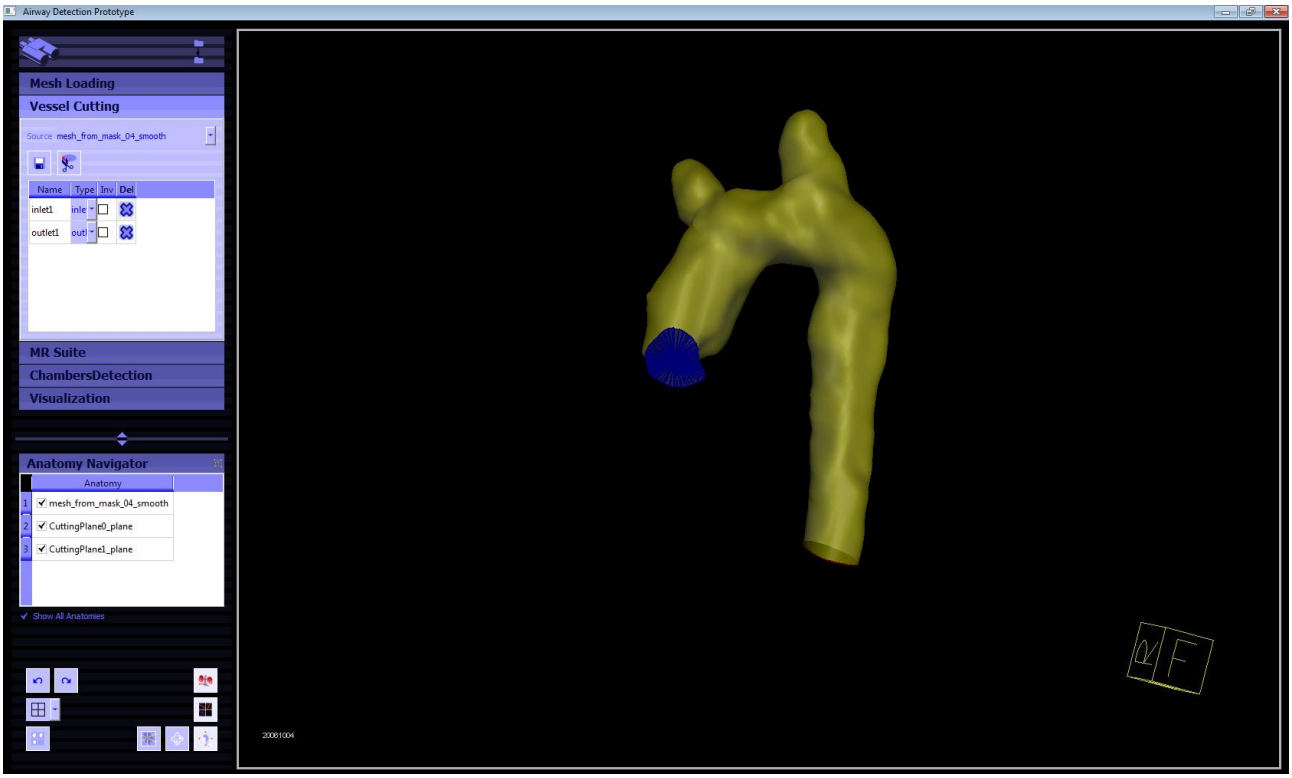

Figure 8 Cutting and tagging (inlet/outlet) of the aortic mesh.

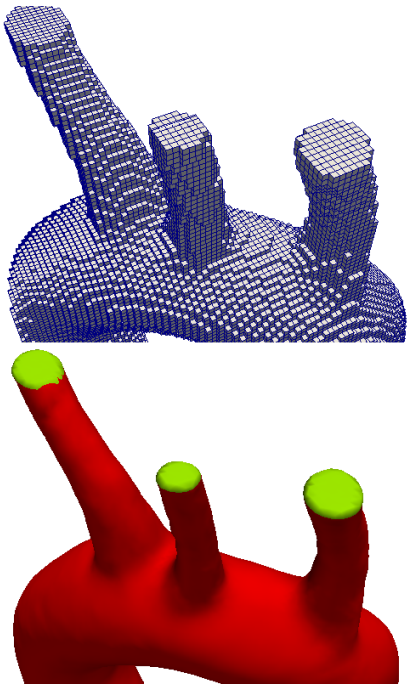

Figure 9 Generic voxelization (top) compared to our approach (bottom).

3. Temporal Propagation of the Aortic Surface Mesh

After segmenting the aorta including the subclavian vessels from a temporal reference time frame, the extracted model is propagated across the entire time sequence using the displacement fields derived from a deformable registration technique in order to obtain a dynamic vascular model, including propagated centrelines and lumen boundary. This method was quantitatively validated in (Gülsün, Jolly, et al. 2012).

4. Establishing velocity initial conditions

Data from 4D PC-MRI can be used as the initial (noisy) measurement which will be enhanced by our algorithm.

5. Estimating inlet and wall fluxes

The measured velocity is used to compute fluxes on the inlet and walls of the vessel. The inlet flux is estimated by filtering a set of several surface flow measurements obtained from sampling the measured velocities on cross-sections of the ascending aorta.

The wall flux can be measured by sampling the velocity at the wall, but PC-MRI wall velocities are noisier than lumen velocities due to partial volume effects, therefore can introduce large measurement errors. A better option is to use wall motion derived from the propagated models above.

6. Estimating outlet flux distribution

Blood vessel outlet flux measurement is usually marred by the low quality of PC-MRI data in outlet regions, due to insufficient resolution (1-3 pixels across) which leads to partial volume effects. As such, the data cannot be used directly to impose absolute flux values.

Instead, one can distribute the fluxes in accordance with the measurements, but scaled such that they add up to the total inlet+wall flux. Alternatively, one can use Murray's law flux distribution between the outlets. At this stage the velocities on the outlet boundary cells are scaled appropriately such that they match the boundary flux conditions, and the flow is preserved. The new velocities and their corresponding fluxes obey (4.3-4.4) in the FCP equations.

7. Solving the Flux-Constrained Poisson (FCP) equations

The system (4.1-4.2) is now a consistent Poisson equation with Neumann boundary conditions in arbitrary geometries, which can be solved using numerical discretization methods.

8. Obtaining the reconstructed velocity field

The reconstructed velocity is obtained by simply plugging in (1) the gradient of the FCP solution. An example of the reconstructed velocity field for 3 patients is shown in Figure 10.

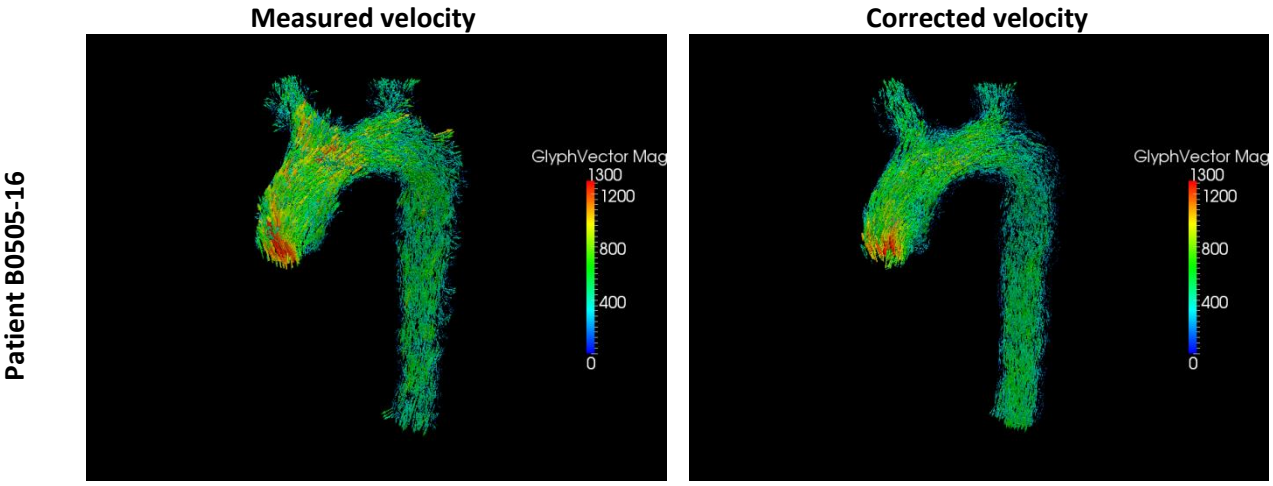

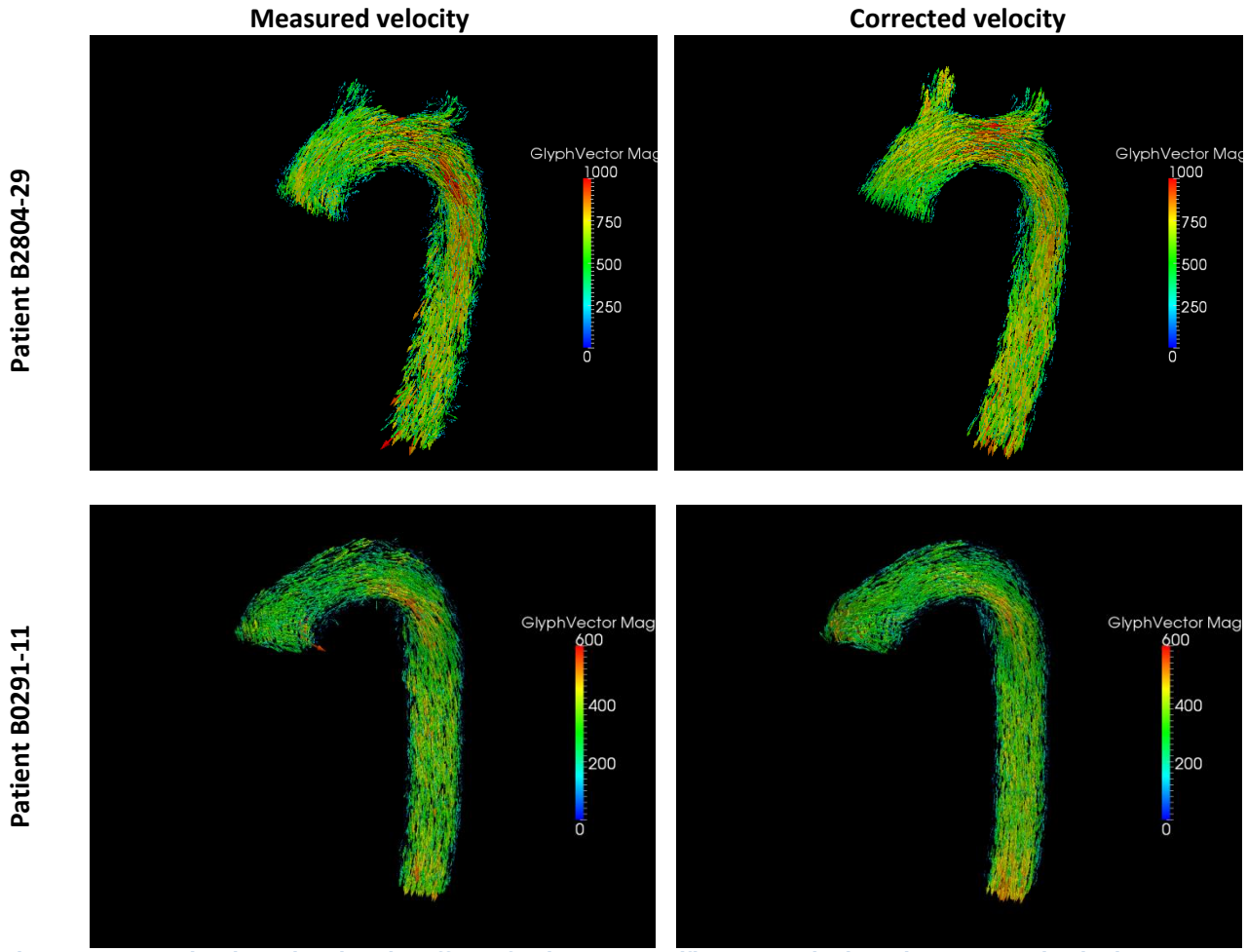

Figure 10 Exemplar data showing the effect of enhancement (flux correction) on the measured velocity.

Quantification of Pressure Maps from Phase-Contrast MRI

Estimation of Relative Pressure from Velocity Fields: Theory

Blood flow in medium sized and larger vessels can be modelled as a Newtonian incompressible fluid obeying the Navier-Stokes equations (Fung 1996):

$$\rho(U_t + (U \cdot \nabla)U) = -\nabla p + \mu \Delta U + \rho F,$$

$$\nabla \cdot U = 0,$$

where t is time, ρ is the fluid density, U=U^{new} is the fluid velocity, U_t refers to the time derivative of U, p is the pressure, μ the fluid viscosity and F are external forces such as the gravity field – which we ignore in a first approximation due to horizontal patient position, which mitigates its effect on measurements. This can be rewritten as

$$\nabla p = RHS$$

$$RHS = -\rho(U_t + (U \cdot \nabla)U) + \mu \Delta U + \rho F\,. \qquad (5)$$

Estimation of Relative Pressure from Velocity Fields: Computation

By taking the divergence of the above pressure equation and considering the normal component to the boundaries we obtain the Pressure Poisson Equations (PPE) and its natural (Neumann) boundary condition:

$$\Delta p = \nabla \cdot RHS$$

$$\frac{\partial p}{\partial n} = RHS \cdot n.$$

After domain initialization using the method introduced in the previous chapter, we find the mean flow in each of the branches of the vessel network and use that as ground truth in terms of flow. Thus, we have a set of 4D tagged meshes with point-correspondence, corresponding 4D grids with tagged cells and nodes (solid/fluid/inlet/outlet), and boundary conditions (estimated flow).

Let us consider the time-varying simply-connected domain *D*, separated into two disjoint subsets D^+ and D^-, such that $D = D^+ \cup D^-$, and *C* is the locally Lipschitz continuous interface between D^+ and D^-. We seek to solve the PPE on the simply connected irregular domain D^- only, and to that end we represent the domain *D* by a level function φ such that $D^- = \{x|\varphi(x) \leq 0\}$, $D^+ = \{x|\varphi(x) > 0\}$ and $C = \{x|\varphi(x) = 0\}$. The level set (Osher und Fedkiw 2001) allows a first order accurate computation for the face fractions used in the discretization of the Laplace operator. In contrast, a staircase approach would have 0^{th} order accuracy.

To find the pressure map we solve the PPE with Neumann boundary conditions at the boundary of an irregular domain using a finite volume discretization of the equations on a staggered grid configuration as shown on Figure 11:

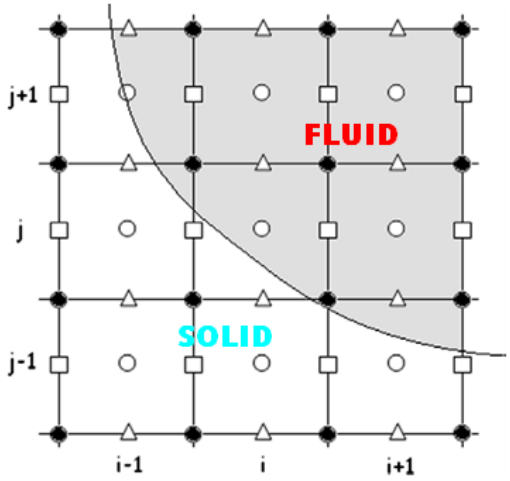

Figure 11 Staggered grid on which the velocities are computed.

In our staggered grid setup the velocity is given at edge centres (*u* on vertical edges and *v* on horizontal ones), while the pressure is given at the cell centres and the level set at the nodes. For flux computation we only need the velocities normal to the cell faces because the flux is measured along the surface normal vector and the tangential flux does not contribute to the cell volume variation. We build the face velocity components starting from the PC-MRI velocity given at cell centres.

Working in a cell C_{ij} and invoking the divergence theorem, we obtain:

$$\int_{C_{ij}\cap D^-} \nabla\cdot\left(\frac{\nabla p}{\rho}\right) dA = \int_{\partial(C_{ij}\cap D^-)} \mathrm{n}\cdot\left(\frac{\nabla p}{\rho}\right) dl$$

Similarly, from the right hand side we get:

$$\int_{C_{ij}\cap D^-} \nabla\cdot RHS dA = \int_{\partial(C_{ij}\cap D^-)} \mathrm{n}\cdot RHS dl$$

Using the level set we can obtain easily approximations for the length fractions for the interfacial faces that we have to deal with in cells like C_{ij}. Namely, for a node-based level set in two dimensions, we get (we write this in 2D for simplicity):

$$L_{i-1/2,j} = \begin{cases} \Delta y \dfrac{\varphi_{i-\frac{1}{2},j-1/2}}{\varphi_{i-\frac{1}{2},j-1/2} - \varphi_{i-\frac{1}{2},j+1/2}} & if\ \varphi_{i-\frac{1}{2},j-1/2} < 0\ and\ \varphi_{i-\frac{1}{2},j+1/2} > 0 \\ \Delta y \dfrac{\varphi_{i-\frac{1}{2},j+1/2}}{\varphi_{i-\frac{1}{2},j+1/2} - \varphi_{i-\frac{1}{2},j-1/2}} & if\ \varphi_{i-\frac{1}{2},j-1/2} > 0\ and\ \varphi_{i-\frac{1}{2},j+1/2} < 0 \\ \Delta y & if\ \varphi_{i-\frac{1}{2},j-1/2} < 0\ and\ \varphi_{i-\frac{1}{2},j+1/2} < 0 \\ 0 & if\ \varphi_{i-\frac{1}{2},j-1/2} > 0\ and\ \varphi_{i-\frac{1}{2},j+1/2} > 0 \end{cases}$$

By approximating the boundary integral on the grid faces as the product of the length and the sampled value at the centre, we obtain:

$$-\int_{\partial(C_{ij}\cap D^-)} \mathrm{n}\cdot\left(\frac{\nabla p}{\rho}\right) \cong \frac{L_{i-1/2,j}}{\rho_{i-1/2,j}}\cdot\frac{p_{i,j}-p_{i-1,j}}{\Delta x} + \frac{L_{i+1/2,j}}{\rho_{i+1/2,j}}\cdot\frac{p_{i,j}-p_{i+1,j}}{\Delta x} + \frac{L_{i,j-1/2}}{\rho_{i,j-1/2}}\cdot\frac{p_{i,j}-p_{i,j-1}}{\Delta y} + \frac{L_{ij+1/2,}}{\rho_{i,j+1/2}} \cdot\frac{p_{i,j}-p_{i,j+1}}{\Delta y} - \int_{C_{ij}\cap C} \mathrm{n}\cdot RHS$$

Similarly one obtains an approximation for $\int_{\partial(C_{ij}\cap D^-)} \mathrm{n}\cdot RHS dl$, and one can put together a symmetric positive definite system to solve the Poisson equation for the pressure:

$$\frac{L_{i-1/2,j}}{\rho_{i-1/2,j}}\cdot\frac{p_{i,j}-p_{i-1,j}}{\Delta x} + \frac{L_{i+1/2,j}}{\rho_{i+1/2,j}}\cdot\frac{p_{i,j}-p_{i+1,j}}{\Delta x} + \frac{L_{i,j-1/2}}{\rho_{i,j-1/2}}\cdot\frac{p_{i,j}-p_{i,j-1}}{\Delta y} + \frac{L_{ij+1/2,}}{\rho_{i,j+1/2}}\cdot\frac{p_{i,j}-p_{i,j+1}}{\Delta y} = L_{i-1/2,j}\cdot RHS^1_{i-1/2,j} - L_{i+1/2,j}\cdot RHS^1_{i+1/2,j} + L_{i,j-1/2}\cdot RHS^2_{i,j-1/2} - L_{i,j+1/2} \cdot RHS^2_{i,j+1/2} - \int_{C_{ij}\cap C} \mathrm{n}\cdot RHS$$

In the above we denoted $RHS = (RHS^1, RHS^2)$, with RHS defined in Equation (5).

Using the above discretization one puts together a symmetric positive definite linear system for the relative pressure, which is then solved iteratively using a multi-grid method. Note that for interior nodes (defined as nodes with only fluid node neighbours, hence with face weights equal to one) one obtains the usual seven-point discretization of the 3D Laplace operator. For computational efficiency the numerical domain is tagged to include only the masked cells and their immediate outside neighbours and uses a sparse matrix representation for the discrete Laplacian. This ensures a computation time of several seconds on single CPU

for usual resolution of 4D flow MRI data sets that were considered, which is essential for fast clinical feedback.

Experiments and Results

Imaging Data Description

In this section we will carry out numerical simulations on 3 patients from DHZB all with aortic valve disease. The patients are further referred to as B0505-16, B2804-29 and B0291-11 in this report. The imaging examinations were executed on a 1.5 Tesla Philips machine. All the scans made were performed using a 5 element torso coil. MRI acquisitions were synchronized to the heart and breathing cycle using prospective ECG-gating and adaptive diaphragm navigator gating.

The imaging protocol included a cine short axis, a cine transversal, a 3D whole heart, 2D Q-flow scans and 4D flow.

- The short axis scan covered the ventricles, valves and aortic arch. The cine transversal covered the heart from the apex of the ventricles to the carotid arteries. For each image sequence of these 2 scans, one heartbeat was divided in 25 time-steps forming the cine image. The typically used sequence parameters were: echo time 1.1 ms, repetition time 3.2 ms; flip angle 30°, field of view 510 mm; parallel imaging with an acceleration factor of 2 (SENSE); and half-Fourier acquired voxel size, 1.2x1.2x2.2 mm^3 (reconstructed to 0.9x0.9x1.1 mm^3). In all time-resolved CMR image sequences over the cardiac cycle the first time-steps correspond to systole.
- The 3D whole heart covered the left ventricle and the aortic arch. It was made in a monophasic (diastole) scan.
- The 2D Q-flows in the Aortic Valve Disease protocol were executed in the LVOT proximal to the valve and just distal to the valve. The VENC used for the scan was dependent from the situation of the disease of the patient. For this scan 1 slice was made with a thickness of 7 mm also divided in 25 time-steps. The typically used sequence parameters were: 2.451 Echo Time, repetition time 3.930; flip angle of 15.

The 4D flow images, consisted in the measurement of the three-dimensional blood flow velocities over the duration of one cardiac cycle using anisotropic 3D segmented k-space with retrospective electrocardiographic gating. The acquired volume covered the thorax from the apex of the heart to the aortic arch in the feet-to-head direction, the external border and spine in the anterior-posterior direction, and the ascending and descending aorta in the right-left direction. Exemplary scan parameters of this sequence were: field of view feet-head 180 mm, anterior-posterior 200-230 mm (depending on the size of the patient), right-left 90-105 mm (depending on number of slices used), acquired voxel 2.5x2.5x2.5 mm^3, flip angle 5°, repetition time 3.9 ms, echo time 2.6 ms, nominal temporal resolution varying with heart rate for 25 cardiac phases, velocity encoding 150 cm/sec. Scan time varied between 8.5 and 14 minutes, depending on size and position of the heart.

Verification of Proposed Methods with Synthetic Experiments

Level-set Based Extrapolation of Velocities for Improved Pressure Computation

If the velocities at the boundaries have poor quality, then one needs to pay particular attention in implementing the numerical discretization of the boundary conditions for the PPE. We used a level-set

based velocity extrapolation method which provides the outer domain velocities that enable calculating the correct boundary fluxes (Aslam 2004).

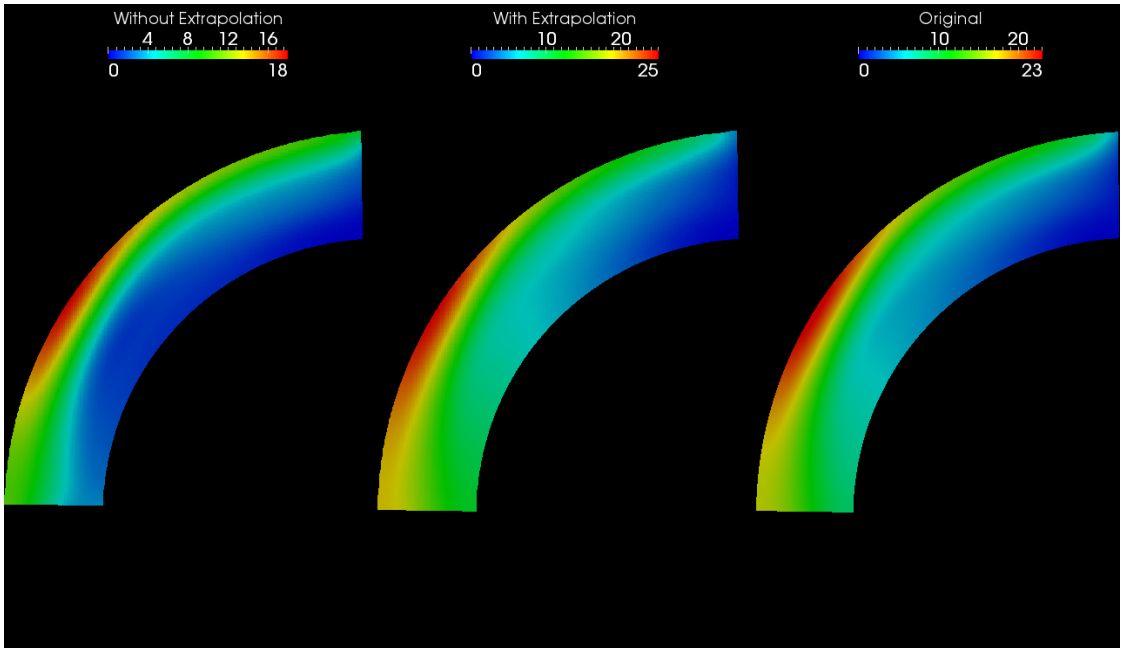

Figure 12 Effects of applying level-set based extrapolation of velocities in the outer domain on pressure computation. Right: the ground truth pressure derived from a CFD simulation. Left: the computed pressure without extrapolation. Middle: the computed pressure with extrapolation. Please notice the different pressure scales (mmHg) used in all three images.

In this experiment, we computed the ground truth pressure (Figure 12, right image) using computational fluid dynamics (CFD) in a standard steady state curved flow experiment at Reynolds number Re = 700 on the inlet. The figure on the left shows the reconstructed results using the approach proposed in this report without applying the level-set based extrapolation of velocities in the outer domain. The middle image demonstrates the effect of applying the level-set based extrapolation. This method allowed an increase in the accuracy of the pressure in this experiment from an L1 error (i.e. the mean absolute error) of approximately 10% to below 3%. Qualitatively, we also notice that the spatial pressure distribution and also drop from inlet to outlet can be recovered quite well.

Robustness in Case of Partially Missing Aortic Domain

It can happen that the whole aortic arch is not properly acquired in the MRI data. This is in particular true for the supra-aortic region which may not be included in the field-of-view, e.g. if the physician is also interested in investigating the lower part of this artery. Such an example is demonstrated in Figure 13.

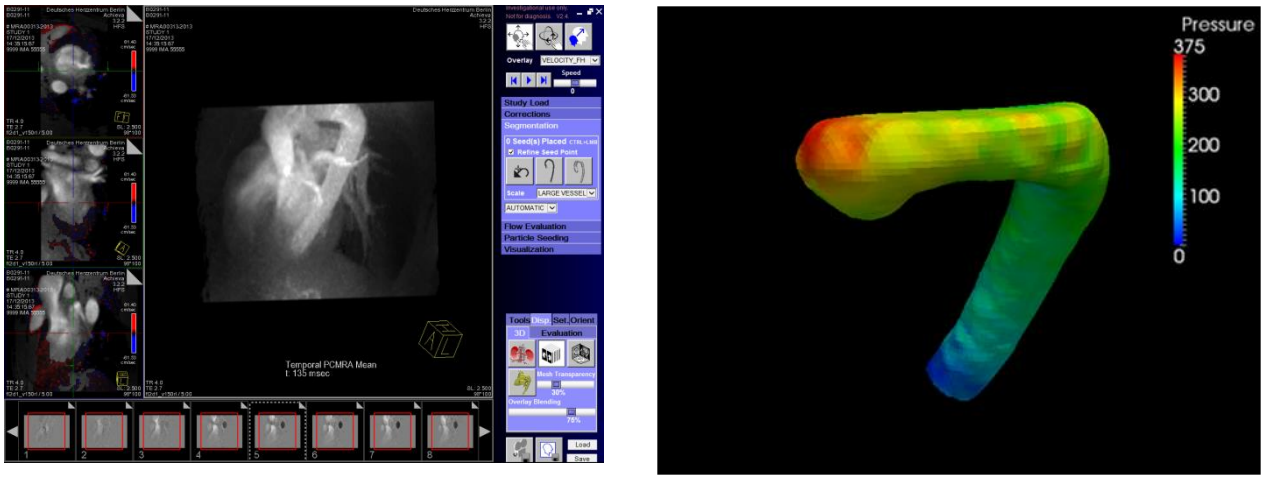

Figure 13: Left: volumetric view of patient B0291-11 showing that the supra-aortic region is missing in the image data. Right: 3D reconstruction of the aorta using the workflow described in the previous section (pressure in Pa).

In this sub-section we would like to investigate if such an incomplete vessel can also be used for simulations and if yes, what is the impact of the missing region on the relative pressure. For this purpose, we selected another patient (B2804-29) with a complete aorta and manually cut the upper part. The simulation pipeline described above was applied to these synthesised data, and the results of the pressure estimation are shown on Figure 14. This figure qualitatively shows that the pressure computation can be reasonably robust on this type of defective data. The error made in such a computation is given by a harmonic function defined on the reduced domain, which is zero on the common boundaries and is equal to the normal part of the divergence free component of the instantaneous acceleration, on the cut region. This can be seen by writing the Hodge-Helmholtz decomposition on both domains, and noting that the difference in the pressure gradients obtained on each of the domains (let's call it DGP) is both a gradient and is divergence free on the common domain, hence harmonic. Furthermore, one has that DGP.n is zero on the common boundary, but non-zero (with zero flux) on the cut boundary. Therefore, the closer to zero DGP.n is, the closer one is to a harmonic function with zero boundary flux, which has zero gradient and the two pressures are the same up to a constant. This specifies that, in particular, the smaller the flux is through the defective (cut) boundary, the smaller the amplitude of the harmonic function (relative to its mean) and the better the reconstruction.

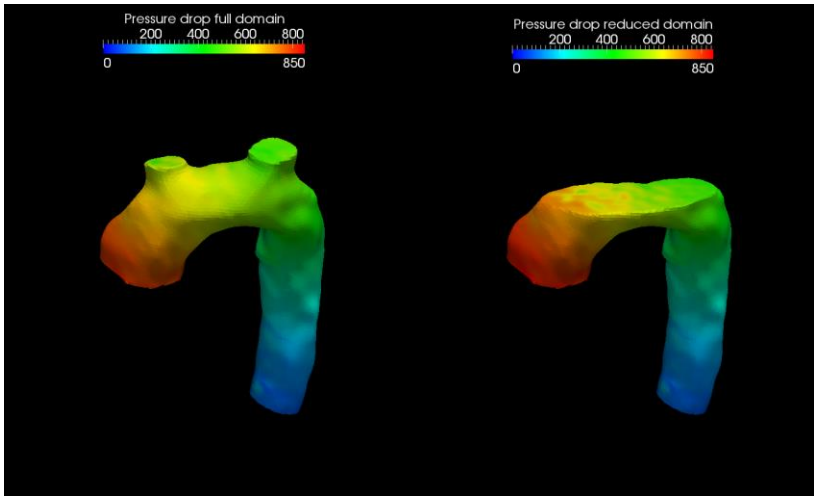

Figure 14 Pressure computation on a synthetically modified aorta (pressure is reported in Pa). Left: pressure drop computed from the original data. Right: pressure drop computed on the manually modified aorta (cut of the supra-aortic region).

Results on clinical data

This section analyses the results of the proposed method on the three patients considered in this report.

Reconstruction of Pressure Maps

Figure 15 shows the computed relative pressures mapped onto the reconstructed 3D meshes of the aorta. The pressure drops in the images are in the physiological range. However, the pressure distribution of patient B0505-16 is atypical, most likely due to the rather erratic velocity distribution in the PC-MRI data, which is in turn likely to be due to a convective inertia dominating the acceleration rather than transient inertia, as usually seen in healthy patients. This happens due to the large spatial gradients of the velocity occurring first in the valve region, which are most likely due to a very pathological bicuspid aortic valve case.

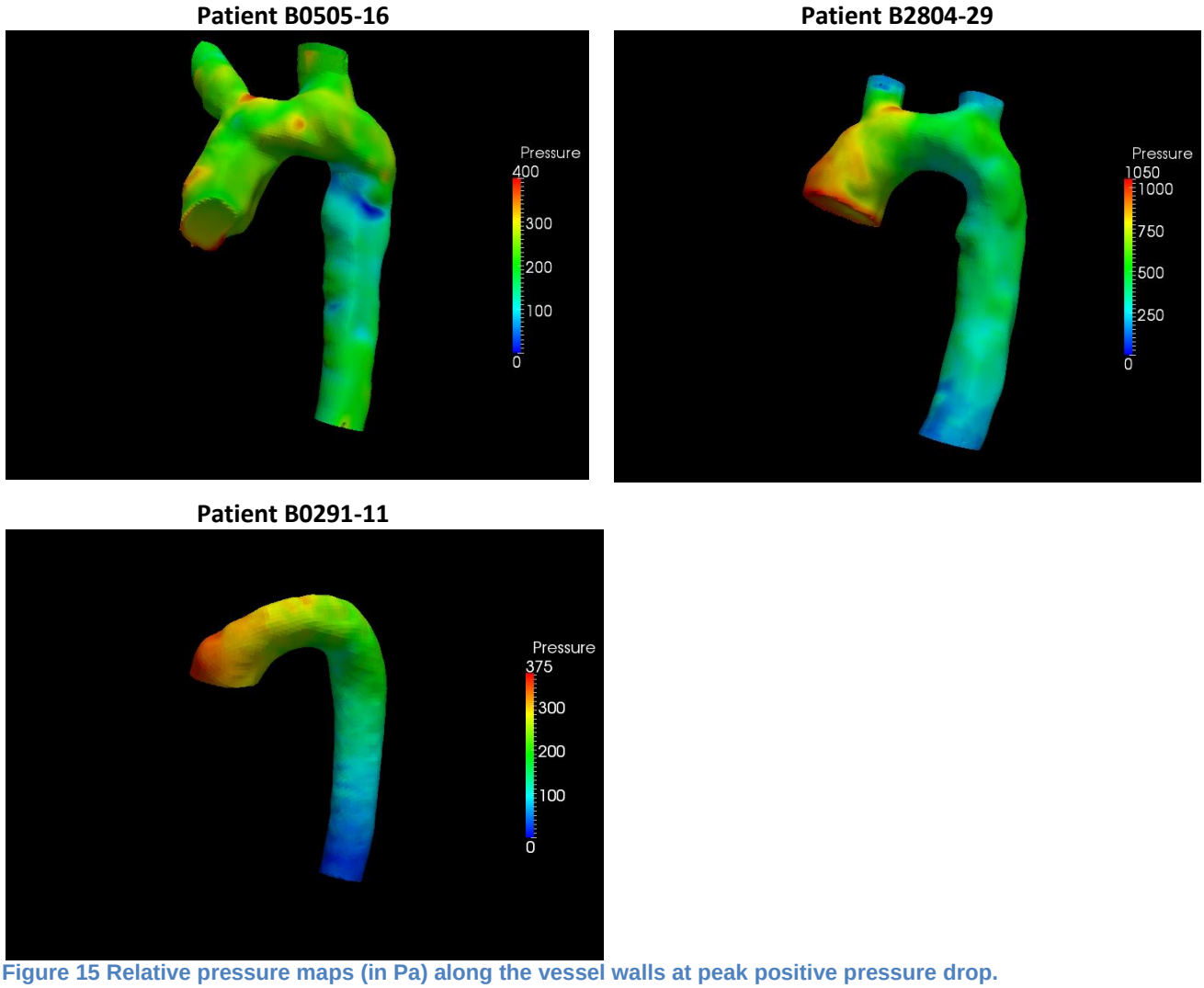

Figure 15 Relative pressure maps (in Pa) along the vessel walls at peak positive pressure drop.

Pressure Drop Curves

Another important source of information used clinically to understand the patient's condition is the drop of relative pressure between the ascending and descending aorta. These curves are shown on Figure 16 for all three patients. The curves confirm that the pressures are in the physiological range (2 – 13 mmHg).The curves look physiological as the drop is typically half of the peak.

However, patient B0505-16 is observed to have a relatively large drop. This may be an indication for aortic regurgitation – which was later on confirmed by our clinical partner. Patient B2804-29 has a low uptake indicating some possible coarctation. We also notice that the first and the last curves have relatively low maximum and minimum pressures drops. It may be an indication that the heart has some deficiencies in pumping. Here, we need to analyze more patient data and work closely with the clinical partners to detect typical patterns in the data which may be useful in influencing the clinical decisions.

Finally, in the first and second plots, we can observe some "plateaux" (between times 4-6 in patient B0505-16 and 6-8 in patient B2804-29). They are numerical artefacts in the estimate of the temporal gradient which are due to the lumen reconstruction not capturing well enough the aortic motion during the end of the systole. While the lumen tracking over time will be enhanced in a subsequent version, the results could still be approximated well by interpolation between the peak and the trough of the pressure graph.

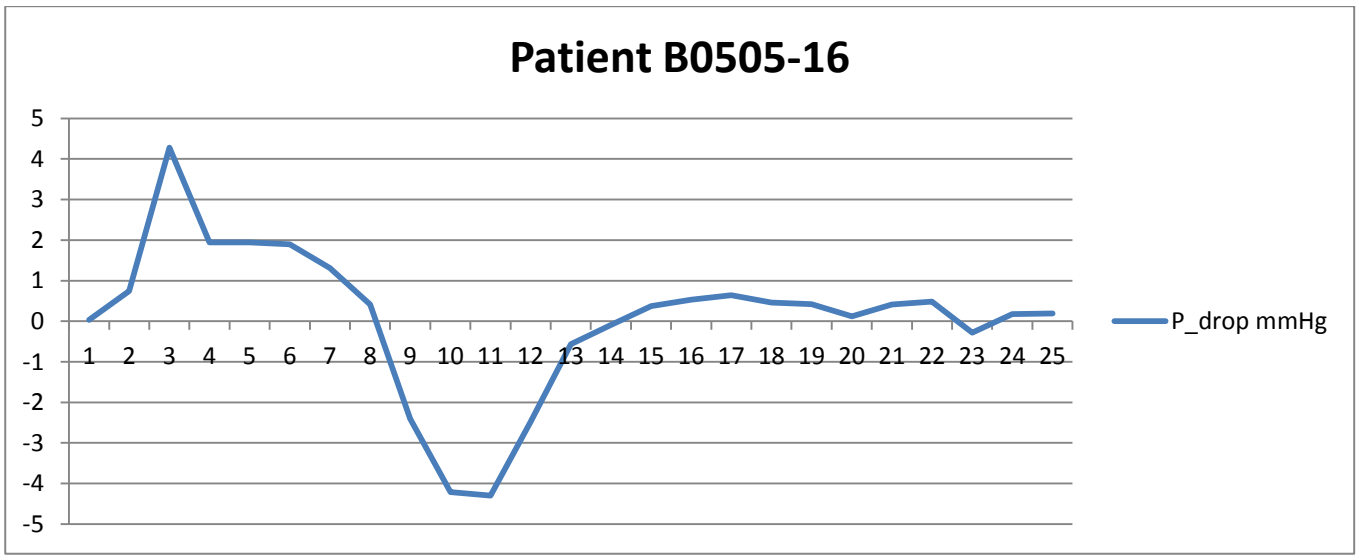

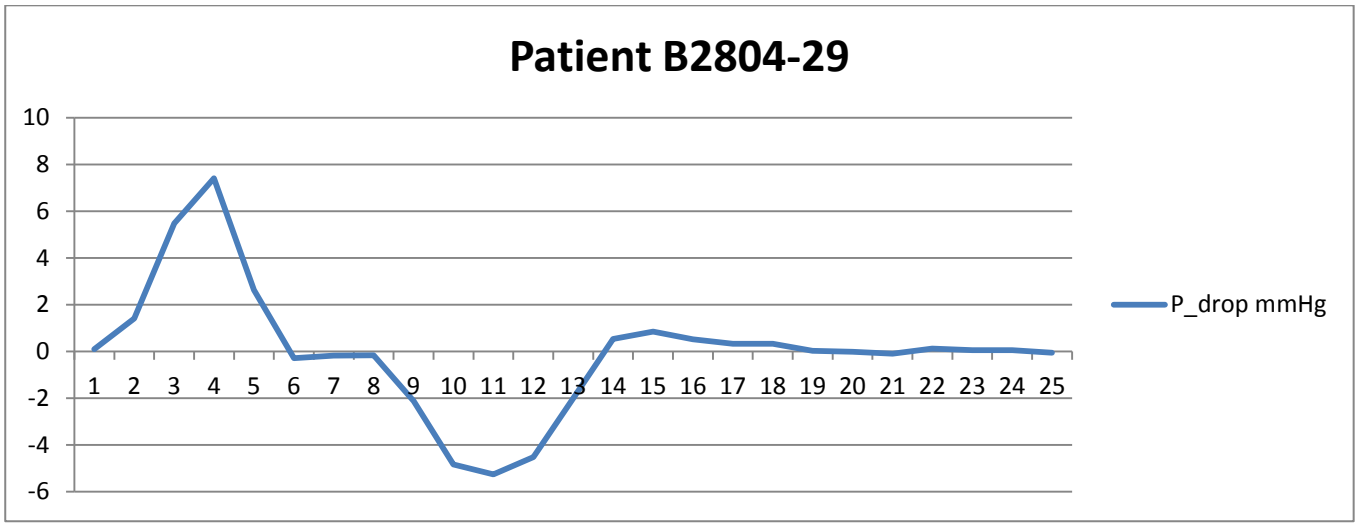

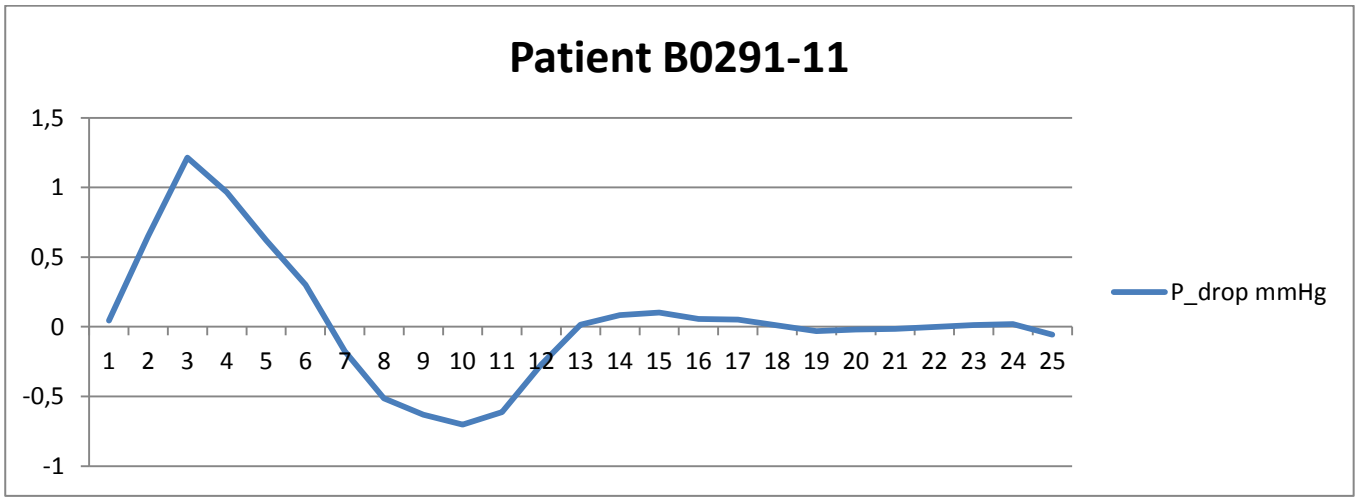

Figure 16 Pressure drop curves: Evolution of the relative pressure between ascending and descending aorta over time.

Total Pressure Drop along Centreline and across a Full Cardiac Cycle

Another interesting and comprehensive representation is a 2D spatiotemporal map of the relative pressure as shown on Figure 17 (Lamata, et al. 2013). In these maps, the relative pressure values are computed alongside the centreline of the aorta at all time steps by subtracting the distal pressure averaged in the most distal cross-section from the averaged actual pressure at each centreline cross-section. This type of representation is useful as it gives at a glance the variation of pressure anywhere in the vessel. It can also be a nice feature that can be used to train machine learning algorithms to support in the decision making process (operate vs. observe) and to predict the outcome of a therapy.

In the curves below, we artificially imposed the most distal relative pressure to be zero. However, to allow a more accurate estimate of the physical value of the actual pressure over time (i.e. along the X-axis), we could couple the distal pressure with the cuff pressure which is also recorded with the image data.

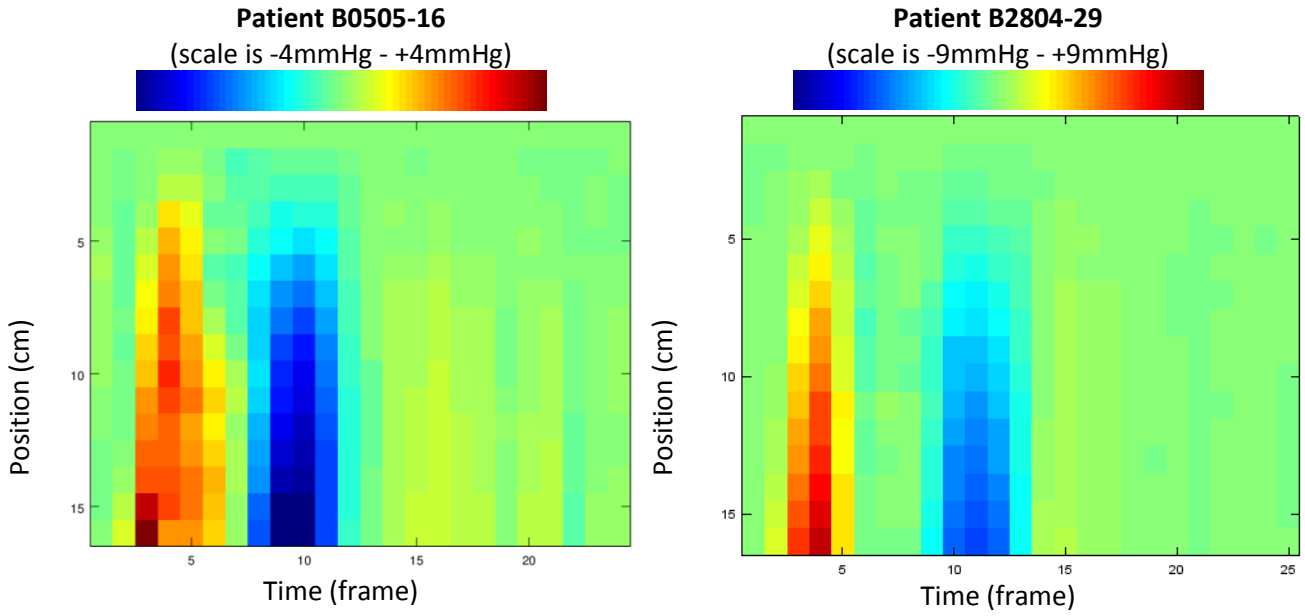

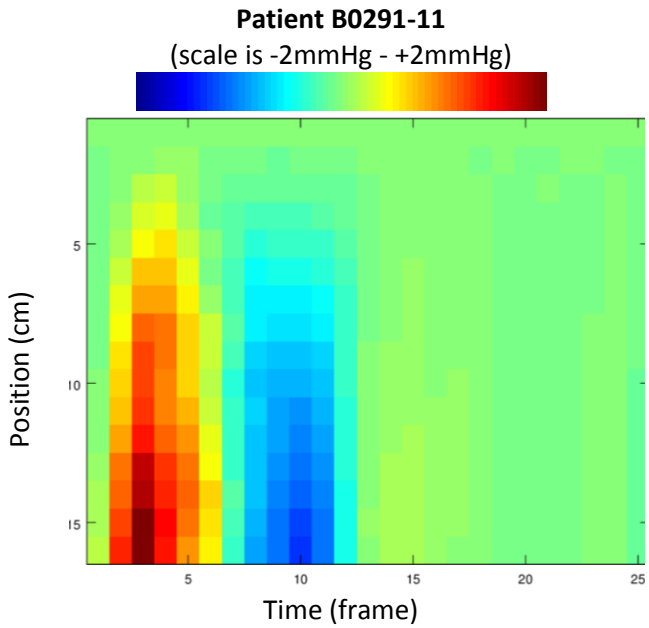

Figure 17 Spatiotemporal maps of relative pressure showing the average pressure alongside the length of the aorta (Y axis, measured in cm away from the descending aorta outlet) through time (X axis). Note that the scale of each pressure component is different.

Computational Time

In this subsection we would like to briefly review the time needed to process a full data set. Although we are at the beginning of the project, it is crucial to always keep an eye on the potential translation of the technology towards a clinical application. All measurements were done on a single Intel Xeon CPU with 2.53GHz frequency and a 64 bit machine.

	Automatic Processing	*Interactive Processing*
Blood Flow Velocity Reconstruction		
Data loading and correction (such background phase correction, VENC anti-aliasing and motion correction)	~ 3-4 minutes	-
Centreline + lumen generation	~ 2 minutes	A few minutes only if automatic method fails
Mesh Preparation		
Mesh smoothing + inlet/outlet cutting	-	~ 5 minutes
Data preparation for pressure computation (level set generation, re-sampling)	~ 5 minutes	-
Pressure map computation		
Solving the equation system for the whole heart cycle	~ 3-4 minutes	-

In summary, the processing of a new case requires about 20 minutes, which we think is already reasonable in terms of clinical requirements.

Conclusions and Outlook

In this report, we showed the feasibility of reconstructing the relative blood pressure from non-invasive velocity measurements acquired by PC-MRI. This technique could be applied to three patients from the CARDIOPROOF project, delivering sound results even with imperfect data. The workflow set in place is relatively straightforward and can be executed within a reasonable amount of time. It will serve as the basis to process the numerous cases which will be acquired throughout the project. Verification of the pipeline against analytic solutions of pipe flow was successfully carried out above and also in (Mihalef, et al. 2014). Moreover, the whole pipeline will be validated using the coarctation cases, also acquired within the project, which include invasive pressure measurements. That way, it will be possible to directly compare the simulated pressures with the measured ones.

The next steps consist of increasing the database of processed patients and validate the proposed approach on a large scale population with the support of the clinical partners involved in the project. Relationships between treatment outcomes and simulation results from this database will be investigated. Finally, the presented workflow will be extended by a coupling interface between fluid and solid that will receive the fluid pressure on the interface nodes from the Computational Fluid Dynamics solver and the displacement of these nodes from the Computational Solid Mechanics solver.

Acknowledgements

The author would like to sincerely thank Viorel Mihalef and Mehmet Gülsün from Siemens Corporation for their support and guidance in preparing this report.

Bibliography

Aslam, Tariq D. “A partial differential equation approach to multidimensional extrapolation.” *Journal of Computational Physics* 193, no. 1 (2004): 349–355.

Bock J., et al. “In vivo noninvasive 4D pressure difference mapping in the human aorta: phantom comparison and application in healthy volunteers and patients.” *Magnetic Resonance in Medicine*, 2011: 1079–1088.

Busch, Julia and Giese, Daniel and Wissmann, Lukas and Kozerke, Sebastian. “Reconstruction of divergence-free velocity fields from cine 3D phase-contrast flow measurements.” *Magnetic Resonance in Medicine* 69, no. 1 (2012): 200-210.

Busch, Julia, Daniel Giese, Lukas Wissmann, and Sebastian Kozerke. “Reconstruction of divergence-free velocity fields from cine 3D phase-contrast flow measurements.” *Magnetic Resonance in Medicine* 69, no. 1 (2012): 200-210.

Currie, P.J., et al. “Continuous-wave Doppler echocardiographic assessment of severity of calcific aortic stenosis: a simultaneous Doppler-catheter correlative study in 100 adult patients.” *Circulation* 71, no. 6 (1985): 1162–9.

Fung, Y C. *Biomechanics: Circulation.* 2nd Edition. Springer, 1996.

Gülsün, M A, and H Tek. “Robust vessel tree modeling.” *Medical Image Computing and Computer-Assisted Intervention (MICCAI).* 2008. 602–611.

Gülsün, M A, et al. “A novel 4D flow tool for comprehensive blood flow analysis.” 2012. Proceedings of ISMRM.

Gülsün, M, and H Tek. “Segmentation of carotid arteries by graph-cuts using centerline models.” *Proc. SPIE 7625, Medical Imaging 2010: Visualization, Image-Guided Procedures, and Modeling.* 2010. 762530.

Krittian, S B, et al. “A finite-element approach to the direct computation of relative cardiovascular pressure from time-resolved MR velocity data.” *Medical Image Analysis* 16, no. 5 (2012): 1029 – 1037.

Lamata, P, et al. “Aortic relative pressure components derived from four-dimensional flow cardiovascular magnetic resonance.” *Magnetic Resonance in Medicine*, 2013.

Markl, M, P Kilner, and T Ebbers. “Comprehensive 4D velocity mapping of the heart and great vessels by cardiovascular magnetic resonance.” *Journal of Cardiovascular Magnetic Resonance* 13, no. 1 (2011): 7.

Markl, M., et al. “Time-resolved 3D MR velocity mapping at 3T: Improved navigator-gated assessment of vascular anatomy and blood flow.” *Journal of Magnetic Resonance Imaging* 25, no. 4 (2007): 824–831.

Meier, S., A. Hennemuth, J. Drexl, J. Bock, B. Jung, and T. Preusser. “A fast and noise-robust method for computation of intravascular pressure difference maps from 4d PC-MRI data.” *Statistical Atlases and Computational Models of the Heart. Imaging and Modelling Challenges.* 2013. 215-224.

Mihalef, V, et al. “Model-Based Estimation of 4D Relative Pressure Map from 4D Flow MR Images.” *Statistical Atlases and Computational Models of the Heart. Imaging and Modelling Challenges.* Springer Verlag, 2014. 236-243.

Osher, S, and R P Fedkiw. “Level set methods: an overview and some recent results.” *Journal of Computational Physics* 169, no. 2 (2001): 463-502.

Song. “Noise reduction in three-dimensional phase-contrast MR velocity measurements.” 1993.

Song, S M, R M Leahy, D P Boyd, B H Brundage, and S Napel. “Determining cardiac velocity fields and intraventricular pressure distribution from a sequence of ultrafast CT cardiac images.” *IEEE Transactions on Medical Imaging* 13, no. 2 (1994): 386-397.

Song, S M, S Napel, G H Glover, and N J Pelc. “Noise reduction in three-dimensional phase-contrast MR velocity measurements.” *Journal of Magnetic Resonance Imaging* 3, no. 4 (1993): 587-596.

Song, S. M., and R. M. Leahy. “Computation of 3-D velocity fields from 3-D cine CT images of a human heart.” *IEEE Transactions on Medical Imaging* 10, no. 3 (1991): 295-306.

Song, SM, and RM Leahy. “Computation of 3-D velocity fields from 3-D cine CT images of a human heart.” *IEEE Transactions on Medical Imaging* 10, no. 3 (1991): 295-306.

Tafti, P D, and M Unser. “On regularized reconstruction of vector fields.” *IEEE Transactions on Image Processing* 20, no. 11 (2011): 3163-3178.

Tafti, P. D., and M. Unser. “On regularized reconstruction of vector fields.” *IEEE Transactions on Image Processing* 20, no. 11 (2011): 3163-3178.

Tafti, P. D., R. Delgado-Gonzalo, A. F. Stalder, and M. Unser. “Variational enhancement and denoising of flow field images.” *2011 IEEE International Symposium on Biomedical Imaging: From Nano to Macro.* 2011. 1061-1064.

Taubin, G. “A signal processing approach to fair surface design.” *Siggraph’95 Conference Proceedings.* 1995. 351-358.